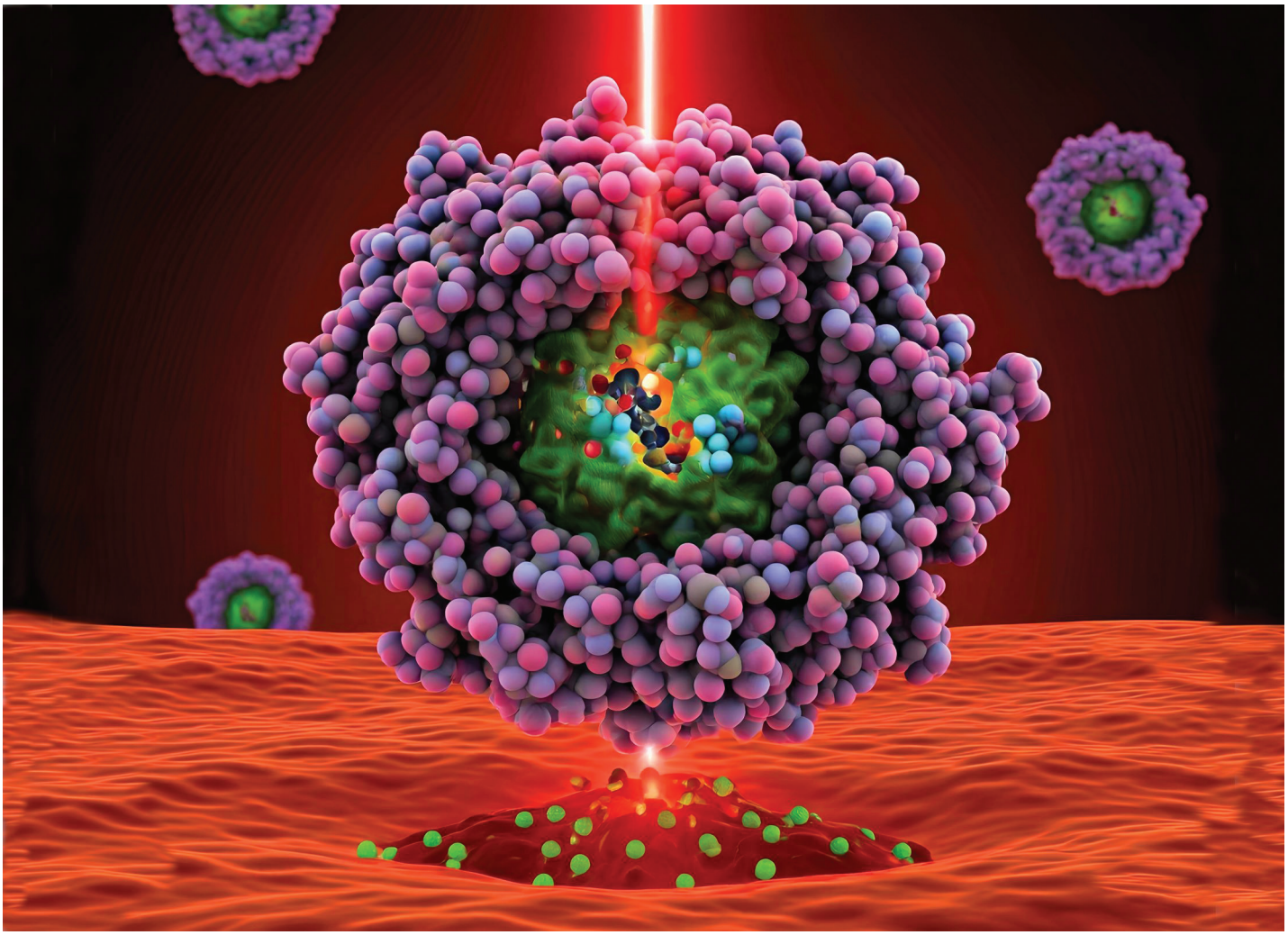

Showcasing research from Professor Sumanta Kumar Sahu's laboratory, Department of Chemistry and Chemical Biology, Indian Institute of Technology (Indian School of Mines) Dhanbad, Jharkhand, India.

Rationally designed porous self-assembled nanoparticles for combinational chemo-photodynamic therapy

This study presents zinc-coordinated quercetin-based self-assembled nanoparticles (ZnQ NPs) for dual-mode cancer therapy, combining chemotherapy with photodynamic therapy. Synthesized in a few minutes, these pH-responsive ZnQ nanoparticles utilize the anticancer properties of quercetin and show excellent water dispersibility and biocompatibility. Loading Chlorin e6 onto nanoparticles improves PDT efficiency by mitigating Chlorin e6 agglomeration. Overall, these innovative nanocarriers have significant potential for improving cancer treatment outcomes through combinational chemo-PDT.

Image generated with Google Gemini.

As featured in:

See Sumanta Kumar Sahu *et al.*, *Dalton Trans.*, 2024, **53**, 17465.

ROYAL SOCIETY OF CHEMISTRY

rsc.li/dalton

Registered charity number: 207890

Dalton Transactions

ROYAL SOCIETY OF CHEMISTRY

PAPER

View Article Online
View Journal | View Issue

Cite this: *Dalton Trans.*, 2024, **53**, 17465

Rationally designed porous self-assembled nanoparticles for combinational chemo-photodynamic therapy†

Kanchan Negi, [a] Ashok Kumar,[a] Gourav Chakraborty, [a] Sudhansubala Sahoo,[a] Sushmita Patra,[b] Niladri Patra, [a] Sujit Kumar Bhutia[b] and Sumanta Kumar Sahu *[a]

Despite notable advancements in cancer therapy, it remains a formidable global health challenge. The emergence of combinational treatments, particularly the integration of chemotherapy with photodynamic therapy (chemo-PDT), offers a glimmer of hope. This study introduces the development of zinc-co-ordinated quercetin-based self-assembled nanoparticles (ZnQ NPs) for advanced dual-mode cancer therapy. These cutting-edge ZnQ nanoparticles were synthesized in a rapid 15-minute single-step process, in stark contrast to the conventional hours or days required. Using Density Functional Theory (DFT) calculations, the optimal binding configurations of ZnQ NPs were precisely determined and further supported by band gap calculations between frontier molecular orbitals. Quercetin, a potent anticancer flavonoid, was used for the first time both as an active drug and as an organic ligand, resulting in pH-responsive nanoparticles with exceptional water dispersibility, stability, and biocompatibility. Additionally, these novel nanoparticles (NPs) were able to load chlorin e6 (Ce6), a photosensitizer known for its high singlet oxygen production, due to hydrophobic interactions within the pores. The ZnQ@Ce6 nanocomposite demonstrated remarkable Ce6 loading (19.03%) and significantly enhanced therapeutic effects, achieving a 77% cell inhibition rate under specific light conditions. This dual-functional platform, enhancing the solubility and bioavailability of Ce6 while harnessing the anticancer properties of quercetin, underscores the potential of ZnQ NPs in clinical nanomedicine, promising improved cancer treatment outcomes.

Received 29th August 2024,
Accepted 2nd October 2024

DOI: 10.1039/d4dt02454k

rsc.li/dalton

1. Introduction

Despite the notable achievements made in cancer treatment in the past decades, cancer is still a global public health issue and continues to seriously threaten human health.[1] Recently combinational therapy has attracted much interest to advance tumor therapeutic efficiency.[2,3] On this subject, diverse combined therapeutic methodologies, such as PDT/PTT, chemo-PDT, and chemo-PTT, have gained much attention due to their benefits, including enhanced anticancer efficacy through dual-mode action, reduced dosages of chemotherapeutic drugs, and decreased drug resistance.[4–7] To date, numerous types of research have been developed with the integration of nanomaterials and small molecules to realize combinational therapy. In the past few years, the combination of PDT and chemotherapy has demonstrated effectiveness in cancer treatment due to their complementary effects. Generally, PDT is employed for cancer therapy by the interaction of specific wavelengths of light with nanostructure materials producing reactive oxygen species (ROS).[8,9] Some combined chemo/PDT systems have been reported by researchers and clinicians for therapeutic purposes.[10–13] However, the reported systems usually needed multistep preparation as well as complicated chemical design processes. So, the development of a robust and facile approach for designing nanostructured materials for combinational chemo/PDT remains a significant challenge.

Quercetin, a flavonoid found in plants, is considered a promising anticancer agent for the therapy of different malignancies with almost no toxic side effects. According to the literature, quercetin shows biological activities, such as antioxidant, anti-inflammatory, antiatherosclerosis, hepatoprotective activities, anticancer and antiproliferative effects, on a

[a]*Department of Chemistry and Chemical Biology, Indian Institute of Technology (ISM), Dhanbad 826004, Jharkhand, India. E-mail: sumantchem@gmail.com, sksahu@iitism.ac.in; Tel: +91 3262235936, +91 7631042241*
[b]*Department of Life Science, National Institute of Technology Rourkela, 769008 Odisha, India*

† Electronic supplementary information (ESI) available. See DOI: https://doi.org/10.1039/d4dt02454k

wide range of human cancer cell lines.[14,15] It has recently been investigated whether the proliferation of many cancer cells is inhibited by quercetin due to the regulation of the expression of tumor-suppressor gene metastasis. Most significantly, at a high concentration level, quercetin possesses little cytotoxicity against normal cells.[16] As a result, quercetin is considered a promising molecule for the therapy of numerous cancers. However, a complication of the use of quercetin in clinical trials involves its poor water solubility, poor stability, rapid metabolism and low bioavailability. Researchers have made many attempts to facilitate its administration using a diversity of drug delivery systems (DDSs) including polymeric gels, nanoparticles, dendrimers, and metal–organic frameworks.[17–19] For example, Jiang *et al.* developed a pH-responsive combinational therapy platform FA-BSA/CuS@ZIF-8-QT with a quercetin drug loading capacity of 24%.[20] Parsaei *et al.* reported the formulation of quercetin-loaded UiO-66-R MOF as a smart nanocarrier for targeted delivery of quercetin.[21] Nguyen *et al.* demonstrated the synthesis of ZIF-8 nanoparticles loaded with quercetin and further modified with hyaluronic acid as a drug delivery system for an enhanced cytotoxicity effect on cancer cells.[22] In all the literature reports, it has been found that quercetin can be encapsulated into nanomaterials for drug delivery purposes. For the first time in this study, we utilized quercetin not only as a drug molecule but also as a ligand to design and synthesize ZnQ nanoparticles. Quercetin was chosen as the organic ligand due to its carbonyl and phenolic hydroxyl groups, which exhibit strong coordination with Zn^{2+}. Taking the amphiphilic and antitumor properties of quercetin into account, we hypothesized that quercetin could be used as a ligand as well as a drug molecule. We thus conceived that the developed NPs can be used as hydrophobic pores for photosensitizer loading. Additionally, the photosensitizer-loaded quercetin-based nanocomposite retains high water dispersibility, making it suitable for both chemotherapy and photodynamic therapy. This dual functionality allows us to effectively address two treatment methods with a single approach.

In recent years, a popular photosensitizer Ce6 has frequently been used for photodynamic therapy of cancer. The advantages of Ce6 as a photosensitizing agent are high $^1O_2$ production, 630–690 nm light-mediated activation, minimal dark toxicity, and fluorescent active molecules for imaging.[23–25] Simultaneously, the disadvantages of Ce6 are poor water solubility and aggregation *via* π–π stacking, which quenches its PDT efficiency. To address these issues, researchers have developed various nanoformulations for Ce6 delivery. For example, Fu *et al.* designed hyaluronic acid-modified ZIF-8 loaded with Ce6 using a one-pot encapsulation method for PDT.[26] Sheng *et al.* constructed a peroxidase mimicking MIL-100 loaded with 17.4% Ce6 for synergistic chemo-PDT.[27] Jia *et al.* developed a pH-responsive MOF nano platform CAB/Ce6@ZIF-8@PEG-FA loaded with cabozantinib and Ce6 for multimodal antitumor therapy. The Ce6 loading content was found to be 13.82%.[28] These studies typically involve the post-synthetic loading of drugs, which can lead to lower drug-loading efficiency. To overcome this limitation, our work incorporates quercetin, an anticancer drug, as a ligand in the design of NPs. We synthesized multifunctional self-assembled ZnQ NPs as nanocarriers for Ce6, achieving a high drug-loading content. Self-assembled NPs have gained increasing attention due to their capability of sustained and controlled drug release. Therefore, we have developed a self-assembly-based Ce6 nanocomposite to improve not only PDT efficiency but also chemotherapy in the physiological environment.

Herein, we designed multifunctional NPs by coordinating quercetin and zinc ions. This will be the first investigation of quercetin-based NPs with defined properties like high dispersibility and stability at room temperature, low toxicity, and easy synthesis. The optimal binding configurations of ZnQ nanoparticles were determined using DFT. Because of the excellent properties of the developed NPs, it is easy to load and deliver the Ce6 molecule which resolves the issue of its low solubility in an aqueous environment. It was observed that 19.03% Ce6 was loaded into the ZnQ NPs and they showed an enhanced drug delivery ability for combinational chemo-photodynamic therapy. Under 635 nm wavelength light radiation at an intensity of 60 mW cm^{-2} exposed for 5 min, Ce6 was able to generate a significant amount of singlet oxygen ($^1O_2$), indicating tumor cell apoptosis during PDT. The final nanocomposite, ZnQ@Ce6, exhibited enhanced cell killing, due to the combined anticancer effects of quercetin and Ce6 under laser irradiation. This drug-based low cost and simple preparation strategy exhibited an effective antitumor potential and might support new intuitions into clinical nanomedicine design for combinational therapy.

2. Experimental section

2.1 Preparation of ZnQ NPs

Firstly, $Zn(CH_3COO)_2{\cdot}2H_2O$ (0.087 g, 0.4 mmol) and $C_{15}H_{10}O_7$ (0.100 g, 0.33 mmol) were dissolved in a mixture of 2 ml of DMF and 12 ml of ethanol. The $Zn(CH_3COO)_2{\cdot}2H_2O$ solution was added dropwise to the $C_{15}H_{10}O_7$ solution under magnetic stirring. The reaction was performed at room temperature (~25 ± 5 °C). The stirring was continued for another 15 min. Finally, the product was centrifuged, washed with DMF several times, and then dried at 70 °C overnight in a hot air oven for further characterization studies.

2.2 Preparation of ZnQ@Ce6 NPs and Ce6 loading study

1 mg of Ce6 was dissolved in 1 ml of DMF away from light at room temperature and 5 mg of ZnQ NPs was dispersed in 10 ml of ethanol under ultrasonication. Then the Ce6 solution (1 mg ml^{-1}) was added to the ZnQ NP solution drop-wise under stirring. The stirring was continued for 12 h. The resultant solution was centrifuged, washed with DMF for the removal of unbound Ce6 molecules, and then stored in a dark environment for further characterization. The successful loading of Ce6 was confirmed using a UV-visible spectrophotometer by measuring the absorbance at 660 nm following a pre-

vious procedure.[29] A calibration curve of Ce6 was employed to calculate the drug loading content (DLC) using the following formula:

$$\mathrm{DLC\,(wt\%)} = \frac{\text{weight of loaded Ce6}}{\text{total weight of ZnQ NPs}} \times 100 \qquad (1)$$

2.3 *In vitro* quercetin and Ce6 release studies

Quercetin and Ce6 release experiments were conducted in an incubator at 37 °C with orbital agitation.[30] Additionally, a pH-responsive drug release investigation was carried out for the synthesized nanocomposite. The release patterns were observed using PBS at two distinct pH levels, pH 7.4 and pH 5.5, to mimic physiological conditions. Initially, 2 mg of the nanocomposite ZnQ@Ce6 was dispersed in 3 ml of PBS at pH 7.4 and pH 5.5. At regular intervals, 2 ml of the supernatant was withdrawn from the solution and replaced with an equivalent amount of fresh PBS to keep the volume constant. The cumulative release of quercetin at both pH levels was obtained by measuring the absorbance intensity at 374 nm based on the calibration curve of quercetin in ethanol. Similarly, for Ce6, the cumulative release was calculated using a similar procedure, measuring the absorbance intensity at 660 nm.

2.4 DFT studies

DFT studies were conducted to identify the preferable binding configuration of quercetin in the self-assembled nanoparticles, using the Gaussian 16 package.[31] To achieve this, gas phase optimization, followed by frequency calculations, was carried out using the B3LYP-D3(BJ) functional,[32–34] coupled with a combination of split valence 6-311+G(d, p),[35–37] and an effective core potential type LANL2DZ basis set,[38] applied to the quercetin molecule and Zn^{2+} ion respectively. For all the optimizations, tight convergence criteria and an ultrafine integration grid were used. Finally, the effect of solvent was estimated *via* single-point energy calculations of the optimized structure with the IEFPCM model with a dielectric constant of 26.24, replicating the experimental 1 : 6 solvent ratio of DMF/ethanol.[39] The temperature was set to its default value of 298.15 K for frequency calculations.

As quercetin has 3 different binding sites, 5 systems were constructed, having 1 (3 systems) and 2 Zn^{2+} (2 systems) ions respectively. Their corresponding optimized structures are shown in Fig. S1 and S2†, respectively. Fig. S1† contains only one Zn^{2+} component, tetrahedrally surrounded by two quercetin ligands. The three structures (Fig. S1(a–c)†) correspond to the three donor sites of quercetin (henceforth termed collectively as Sys1). Fig. S2,† conversely, contains a bridged ligand, simultaneously attached to two Zn^{2+} ions. Here the binding regions for quercetin are Site1 + Site3 (Fig. S2a†) and Site2 + Site3 (Fig. S2b†) (hereafter termed collectively as Sys2). The objective was to assess the relative energies of the three binding poses, and how their stability order varies upon increasing the cluster size.

2.5 Cell experiment

HEK293T cells and HeLa cells were procured from NCCS (National Centre for Cell Science), Pune, and cultured in Dulbecco's modified Eagle's medium, enriched with 1% antibiotics (penicillin/streptomycin, 100 μg ml^{-1}) and 10% fetal bovine serum (FBS). They were incubated at 37 °C under a 5% CO_2 atmosphere.

2.6 *In vitro* fluorescence microscopy

The temporal uptake of ZnQ@Ce6 was examined in HeLa cells. Initially, the cells were seeded onto poly-D-lysine-treated glass coverslips at a count of 25 000 cells per well and allowed to adhere for 48 hours. Subsequently, the cells were treated with 50 μg ml^{-1} of the ZnQ@Ce6 nanocomposite and free Ce6, then incubated for 1.5, 3, 6, and 12 hours at 37 °C. After each specified incubation period, the cells were fixed with 4% formaldehyde for 10 minutes at room temperature. They were then washed with PBS, and the coverslips were mounted onto glass slides using Fluoromount-G containing DAPI mounting medium. A Leica fluorescence microscope was used for capturing cellular images.

2.7 *In vitro* cytotoxicity assay

The MTT assay was employed to assess the cytotoxic effects of ZnQ NPs, ZnQ@Ce6, free quercetin, and Ce6 on HeLa and HEK293T cells. Initially, the cells were seeded at a count of 10^4 cells per well in a 96-well plate and allowed to adhere for 24 hours. Subsequently, various doses (0, 12.5, 25, 50, 100, and 200 μg ml^{-1}) of nanocomposites ZnQ NPs, ZnQ@Ce6, quercetin, and chlorin e6 were added to the wells. After a 12 hour incubation period, half of the nanocomposite-treated cells were exposed to 5 minutes of irradiation with a laser of 635 nm wavelength at an intensity of 60 mW cm^{-2}. The 96-well plate was further incubated at 37 °C for 4 hours, after which 25 μl of MTT solution (5 mg ml^{-1} in PBS) was added to each well. The formazan crystals were dissolved by adding 100 μl of DMSO after the MTT-containing medium was removed. A Multiskan FC microplate reader was used to determine the formazan dye absorbance at 450 nm.

2.8 Detection of $^1O_2$ species

To monitor the generation of $^1O_2$ species, we employed the chemical probe DPBF (1,3-diphenyl-isobenzofuran). ZnQ NPs and ZnQ@Ce6, dissolved in PBS at a concentration of 50 μg ml^{-1}, were mixed with a 0.5 mM DPBF solution (100 μl). The mixture was then irradiated with a laser of wavelength 635 nm. The absorption intensity of DPBF at 412 nm was measured at 10-second intervals. The presence of $^1O_2$ led to a pyranoid ring opening and a subsequent decrease in the absorption intensity of DPBF at 412 nm.

2.9 Intracellular $^1O_2$ generation studies

The generation of $^1O_2$ was assessed by employing DCFH-DA, a non-fluorescent compound that undergoes a reaction with $^1O_2$, resulting in the formation of fluorescent 2′,7′-dichlorofluores-

cein (DCF).[40] Before being incubated for a full day, HeLa cells were first seeded at a count of 5000 cells per well in a 96-well plate. Subsequently, 50 μg ml^{-1} of ZnQ NPs, ZnQ@Ce6, and free Ce6 were injected into the cells, which were further incubated for 24 hours. Each well was then filled with a 10-micromolar solution of DCFH-DA in DMEM, and it was left to incubate for ten minutes. Following the incubation period, the medium containing DCFH-DA was removed, and two PBS washes were performed on the cells. Following exposure to a 635 nm laser, the cells were examined under a fluorescence microscope to record photos of DCF fluorescence, which denotes the formation of singlet oxygen.

2.10 Cell apoptosis assay

For the cell apoptosis assay, HeLa cells were cultured in 6-well plates (5×10^4 cells per well) and treated with 50 μg ml^{-1} of the samples in five different groups: (1) control, (2) *hν*, (3) free Ce6 + *hν*, (4) ZnQ@Ce6, and (5) ZnQ@Ce6 + *hν* for 10 h. For the *hν* -related group, the cells were exposed to a 635 nm laser (intensity 60 mW cm^{-2}) for 5 min after being washed with PBS. Subsequently, all cells were stained with calcein AM and EthD-III for 45 min and imaged with a Leica fluorescence microscope. Calcein AM is a non-fluorescent esterase substrate that permeates cell membranes and is converted by esterase in live cells, producing the green fluorescent dye calcein. Ethidium homodimer III (EthD-III) is a DNA dye that cannot pass through intact plasma membranes of viable cells but penetrates dead cells with compromised membranes, staining the nucleus with bright red fluorescence.

2.11 Flow cytometry

HeLa cells (2×10^5 per well) were cultured in a six-well plate at 37 °C under a 5% CO_2 atmosphere for 24 h to assess the type of cell death. Following this, the cells were treated with 50 μg ml^{-1} ZnQ NPs and ZnQ@Ce6 and incubated for an additional 10 hours. For the laser-treated group, the cells were exposed to a 635 nm laser, 60 mW cm^{-2} for 5 minutes. After this, the cells were trypsinized and resuspended in pre-cooled PBS followed by centrifuging for 5 min. Subsequently, the pellet was resuspended in ice-cold 1× binding buffer and incubated with Annexin V-FITC and PI for 20 min at room temperature in the dark. Finally, the cells were acquired in BD LSRFortessa TM and analyzed using BD FACSDiva^{TM} software.

3. Results and discussion

3.1 Synthesis and characterization of ZnQ@Ce6

The synthetic procedure for ZnQ@Ce6 is shown in Scheme 1. As depicted, firstly ZnQ NPs were synthesized using Zn $(CH_3COO)_2{\cdot}2H_2O$ and quercetin in a single-step process at room temperature. Then Ce6 was loaded on the surface of ZnQ NPs resulting in ZnQ@Ce6. The photographic images of the synthesized nanocomposites, namely ZnQ NPs and ZnQ@Ce6, are presented in Fig. S3.† Here, quercetin serves as both a ligand and a drug utilized in anticancer therapy. Quercetin can bind with metal ions through the complexation sites located at the positions O3/O4, O4/O5, and O3′/O4′ (Fig. 1). Typically, complexation between quercetin and zinc occurs at the O3/O4 positions[41,42] as shown in Fig. S4.† The low solubility of quercetin in water limits its effectiveness in cancer treatment.[43] However, incorporating quercetin as a ligand in ZnQ NPs can overcome this limitation, enhancing its potential as an anticancer drug. Fig. S5† presents the solubility test results for free quercetin and the ZnQ NPs, demonstrating the significantly

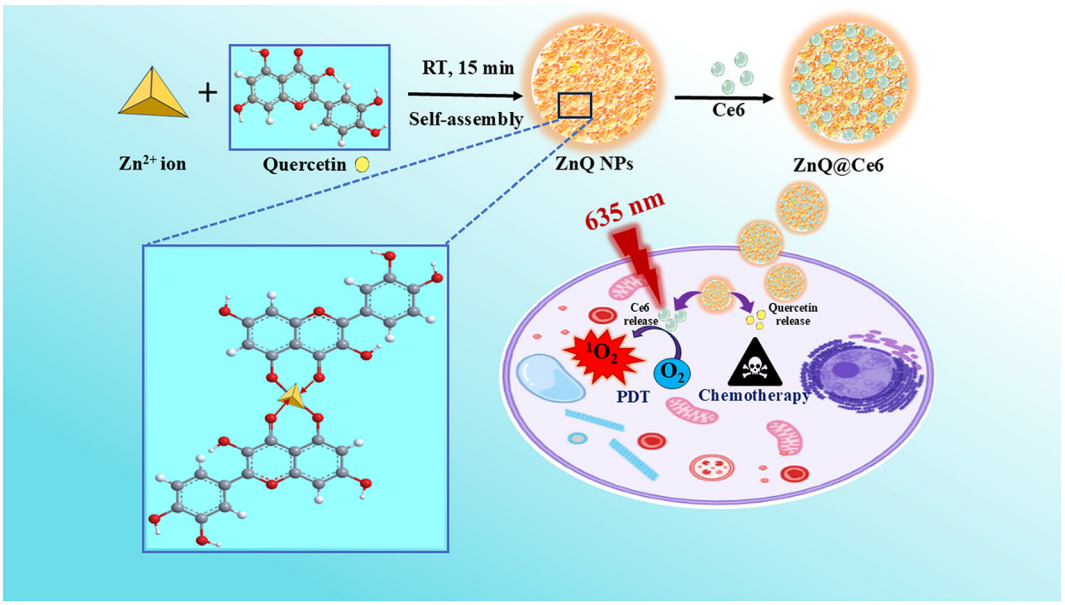

Scheme 1 Illustration of combinational chemo/PDT of ZnQ@Ce6.

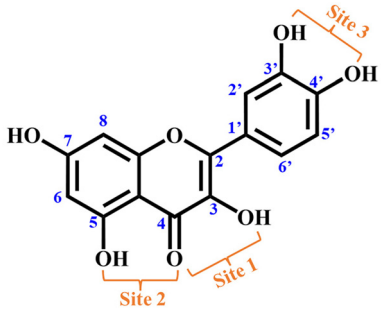

Fig. 1 Complexation sites of the quercetin molecule.

higher solubility of ZnQ NPs in water. This improvement paves the way for its use in biological applications.

3.2 Structural properties of ZnQ NPs and ZnQ@Ce6

FESEM and TEM analyses were employed to characterize the fundamental morphology and average particle size of ZnQ NPs and ZnQ@Ce6 NPs. Fig. 2a and b depict the FESEM images of ZnQ NPs and ZnQ@Ce6, respectively, showcasing similar morphological features. The size distribution graphs in Fig. 2c and d reveal that the nanomaterials have an average particle size of 118 nm, facilitating their internalization through cell-receptor-mediated endocytosis. Subsequent TEM images are given in Fig. 3a and b. In Fig. 3c, the hydrodynamic diameters of ZnQ NPs and ZnQ@Ce6 determined *via* Dynamic Light Scattering (DLS) appear slightly larger than those obtained from TEM and FESEM images. Specifically, the DLS analysis revealed sizes of 165 ± 5 nm for ZnQ NPs and 172 ± 5 nm for ZnQ@Ce6. This disparity in size measurements can be attributed to the differing principles of the techniques employed. DLS assesses the hydrodynamic diameter of nanoparticles in an aqueous solution, capturing their swollen state, whereas SEM and TEM measure the sizes of nanoparticles in their dry form. As a result, the nanoparticles in their dry state exhibit notably smaller particle sizes compared to their suspension in an aqueous medium. Elemental analysis and EDX spectra verified the presence of distinct elements in the nanocomposites ZnQ NPs (Fig. S6†) and ZnQ@Ce6 (Fig. S7†). Carbon (C), zinc (Zn), and oxygen (O) were identified in the EDX spectrum of ZnQ NPs, while an additional peak corresponding to nitrogen (N) was observed in the EDX spectrum of ZnQ@Ce6. Notably, no peak indicative of other elements was detected, indicating the high purity of the synthesized nanocomposite, devoid of any impurities.

Additionally, the XRD spectra analysis of both ZnQ NPs and ZnQ@Ce6 revealed broad peaks indicative of their amorphous nature (Fig. 3d). This observation supports the notion that the loading of Ce6 did not alter the inherent amorphous characteristics of ZnQ NPs. The amorphous nature of ZnQ NPs was further validated by the diffused rings seen in the SAED pattern in Fig. S8.†

3.3 Optical properties of ZnQ NPs and ZnQ@Ce6

The absorption spectra of newly synthesized amorphous ZnQ NPs, ZnQ@Ce6, quercetin, and Ce6 are given in Fig. 4a Initially, the distinctive absorption bands of quercetin, characterized by $\pi \rightarrow \pi^*$ transitions in the B-ring (Band I) at 374 nm and a combination of transitions in the A-ring (Band II) at

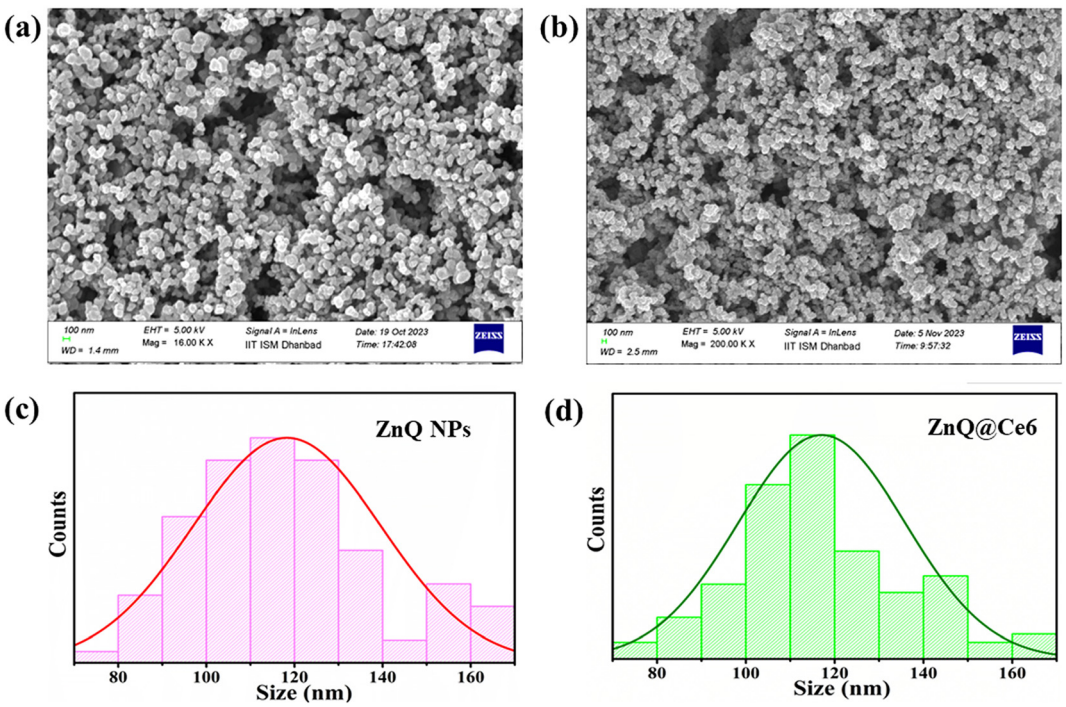

Fig. 2 FESEM images of (a) ZnQ NPs and (b) ZnQ@Ce6, and size histograms of (c) ZnQ NPs and (d) ZnQ@Ce6.

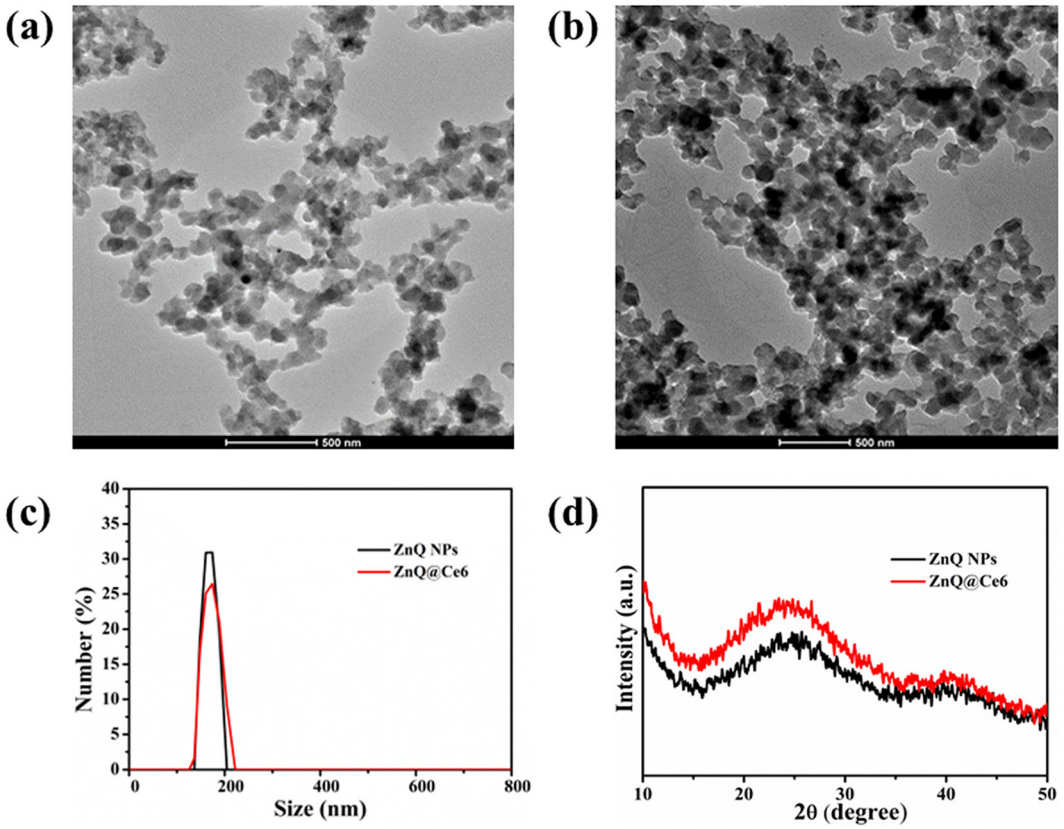

Fig. 3 TEM images of (a) ZnQ NPs and (b) ZnQ@Ce6, (c) DLS size distribution, (d) XRD pattern of ZnQ NPs and ZnQ@Ce6.

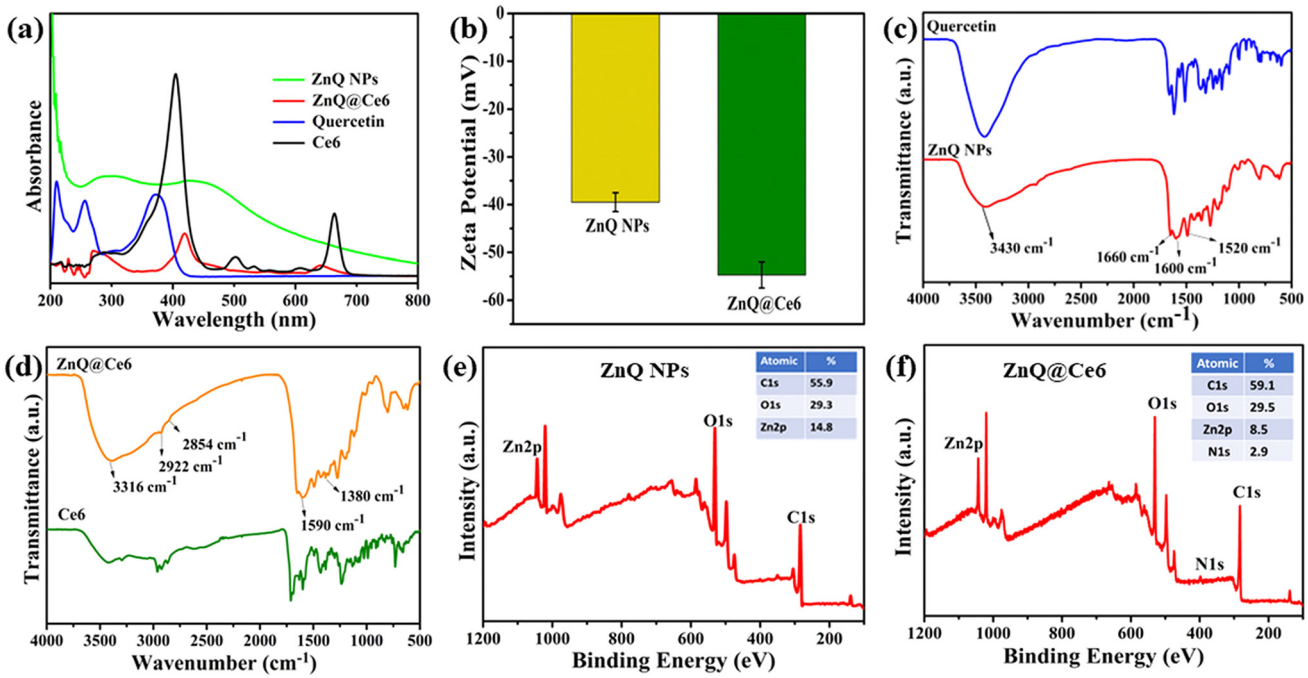

Fig. 4 (a) UV-vis absorbance spectra of quercetin, Ce6, ZnQ NPs, and ZnQ@Ce6. (b) Zeta potential of the as-synthesized ZnQ NPs and ZnQ@Ce6. FTIR spectra of (c) quercetin and ZnQ NPs, (d) Ce6 and ZnQ@Ce6. XPS survey of (e) ZnQ NPs, and (f) ZnQ@Ce6.

255 nm, set a baseline for comparison.[44] When compared to free quercetin, ZnQ NPs shows a strong bathochromic shift due to a B ring absorption at 440 nm. In addition, there is a short bathochromic shift in the A ring absorption band at 292 nm when compared to pure quercetin. Due to the higher conjugation of the Zn(II)-quercetin system caused by the development of the metal–oxygen bond in ring C and the participation of the OH group in chelation, there has been a substantial bathochromic shift to a longer wavelength of Band I compared to that of free quercetin.[45] The absorption spectra of free Ce6 molecule exhibit a characteristic peak at 660 nm while ZnQ@Ce6 shows absorption peaks of Ce6 with some hypsochromic shift indicating that Ce6 was successfully loaded onto ZnQ NPs. The synthesized ZnQ NPs and ZnQ@Ce6 were stable in PBS (pH 7.4) which significantly raised the potential for their use in *in vitro* applications (Fig. S9†).

3.4 Zeta potential, Fourier transform infrared study, and X-ray photoelectron spectroscopy

The surface charge of nanocomposites was examined using zeta potentials as shown in Fig. 4b. The zeta potentials of ZnQ NPs and ZnQ@Ce6 were −39.5 mV and −54.7 mV respectively. The fluctuation in zeta potential is in good agreement with the negative charge attribute of both quercetin and chlorin e6. The zeta potential of ZnQ@Ce6 decreased as compared to that of ZnQ NPs due to the negative charge of chlorin e6, confirming the loading of Ce6 on ZnQ NPs.

Additionally, FT-IR spectra of various samples were systematically acquired to elucidate the synthesis processes, as depicted in Fig. 4c and d. Pure quercetin and pure Ce6 molecules were analyzed as controls. The stretching vibrations of OH/NH are represented by the wide peak detected between 3000 cm^{-1} and 3600 cm^{-1}, whereas the stretching bond vibration of C=O is responsible for the peak at 1670 cm^{-1}.[46] Peaks at 2922 and 2854 cm^{-1}, respectively, in the FTIR spectra of Ce6 and ZnQ@Ce6, signify the presence of the C–H bond in the methyl or methylene group of the Ce6 molecule, hence verifying its presence in the ZnQ@Ce6 nanocomposite. A characteristic peak at 1590 cm^{-1} in the FTIR spectra of ZnQ@Ce6 was observed to be strengthened and broadened simultaneously, attributed to the C–O vibration and the O–H vibration from the carboxyl group. This observation confirms the successful loading of Ce6 into ZnQ NPs to form ZnQ@Ce6.[26] Additionally, some quercetin-related peaks in the spectra of ZnQ NPs and ZnQ@Ce6 demonstrated that quercetin had been successfully incorporated into the nanoparticles. The O–H vibration in the spectrum of quercetin is represented by the wide band between 3360 and 3460 cm^{-1}, whereas the C=O stretching vibration is linked to the distinctive peak at 1660 cm^{-1}. For the C=C stretching vibration, peaks at 1600 and 1520 cm^{-1} are observed. These results suggest that quercetin binds to zinc metal ions *via* its OH functionality and that quercetin's oxo and hydroxyl groups aid in the coordination and chelation of different metal ions.[47]

Moreover, XPS analysis was conducted to delve into the structural properties of ZnQ NPs and ZnQ@Ce6. In the XPS survey of ZnQ NPs, peaks corresponding to C 1s, O 1s, and Zn 2p were observed at 285 eV, 532.61 eV, and 1044.28 eV, respectively (see Fig. 4e and f). In the XPS survey scan of ZnQ@Ce6, an additional peak for N 1s was observed at 398.80 eV, confirming the successful loading of Ce6 onto ZnQ NPs.[48] The survey scan revealed that carbon, oxygen, and zinc are the main constituents of ZnQ NPs present in the ratios of 55.9%, 29.3%, and 14.8%, respectively, whereas in ZnQ@Ce6 carbon, oxygen, zinc, and nitrogen are present in the ratios of 56.0%, 26.0%, 16.1%, and 1.9%, respectively. The HR-XPS spectra for ZnQ NPs and ZnQ@Ce6 are provided in Fig. S10.† The high-resolution C1s spectrum revealed three types of carbon, including C–C/C=C (283.54 eV), C–O (285.06 eV), and C=O (287.57 eV) groups. Three types of oxygen were identified from the high-resolution O 1s spectrum: Zn–O (528.89 eV), C=O (530.59 eV), and C–OH (531.86 eV) groups. Additionally, the HR-XPS spectrum of Zn 2p was deconvoluted into Zn 2p3/2 (1021.11 eV) and Zn 2p1/2 (1044.21 eV).[49] For ZnQ@Ce6, the N 1s XPS spectrum can be divided into three peaks corresponding to N–H (397.00 eV), C–N (398.83 eV), and C=N (400.72 eV) groups. Comparing the HR-XPS spectra of ZnQ NPs and ZnQ@Ce6, slight shifts in the peak positions of C 1s, O 1s, and Zn 2p in ZnQ@Ce6 are observed, likely indicating the successful loading of Ce6 onto the surface of ZnQ NPs. These XPS results align with the findings from FTIR analysis.

3.5 BET analysis

Surface area analysis was conducted to explore the specific surface area and porosity of the newly synthesized self-assembled ZnQ NPs. The N_2 adsorption–desorption isotherms for ZnQ NPs and ZnQ@Ce6 are depicted in Fig. S11.† The surface area of ZnQ NPs was determined to be 43.0645 $m^2\ g^{-1}$, and the pore volume was 0.2003 cc g^{-1}. In contrast, ZnQ@Ce6 exhibited a reduced surface area of 26.7024 $m^2\ g^{-1}$ and a decreased pore volume of 0.0925 cc g^{-1}. The incorporation of Ce6 into ZnQ NPs led to reductions in both specific surface area and pore volume, indicating successful binding of Ce6 to the ZnQ NPs. The absorption spectra of the Ce6 solution before and after synthesizing ZnQ@Ce6 are presented in Fig. S12.† The Ce6 loading rate of ZnQ@Ce6 was computed to be 19.03% based on the Lambert–Beer law. The particular absorbance peaks of the ZnQ@Ce6 supernatant weakened in comparison with the pure Ce6 solution. Additionally, the distinct absorption peak at 660 nm of Ce6 shifted noticeably, potentially due to interferences from the synthesized ZnQ@Ce6. These findings suggest that a portion of the Ce6 molecules was successfully loaded into the ZnQ NPs. MD simulations were carried out to determine the nature of interactions between the Ce6 moiety with ZnQ NPs and it can be concluded that the entire assembly of ZnQ@Ce6 is predominantly stabilised *via* van der Waals forces (Fig. S13†).

3.6 TGA analysis

Thermogravimetric analysis (TGA) was used to investigate the thermal stability and the creation of nanocomposites. Fig. S14† shows the TGA curves for ZnQ NPs and ZnQ@Ce6.

The first weight loss at 100 °C was ascribed to the adsorbed water molecules being released from the pores of both ZnQ NPs and ZnQ@Ce6. The subsequent disintegration of the chemical bonds of the nanoparticles was revealed by their degradation at 200 °C. The weight loss between 200 °C and 600 °C indicated that oxygen-containing functional groups were breaking down. The final weight loss seen at 600 °C showed that the NPs had completely broken down. Notably, the TGA profiles for ZnQ NPs and ZnQ@Ce6 showed comparable thermal stability, tolerating losses of total weight of 57% and 66%, respectively, and temperatures as high as 700 °C.

3.7 Binding energies *via* DFT calculations

Firstly, frequency calculations yielded no imaginary values, indicating that all the structures are in their respective ground states. For Sys1 and Sys2, the relative order of energies for the three systems is shown in Fig. 5a and b respectively. As shown in Fig. 5a, the most stable configuration is for Mode 2, which corresponds to the binding of quercetin *via* Site 2. This is followed by Mode 1 (for Site 1), which is destabilized relative to Mode 2 by 3.89 kcal mol^{-1}. The least stability is observed for Mode 3 (for Site 3), which is located 19.23 kcal mol^{-1} above Mode 2. The significant destabilization for Mode 3 indicates that the presence of a carbonyl donor is crucial to stabilize its complex with Zn^{2+}.

While comparing the bond lengths, it was observed that the Zn–O4 bond was lowered from 1.96 Å in Mode 1 to 1.92 Å in Mode 2, implicating a stronger interaction with the carbonyl group in the latter. Also, a decrease of the bond length between Zn^{2+} and hydroxyl oxygen was observed in Mode 2 (2.10 Å), when compared with Mode 1 (2.14 Å). Finally in Mode 3, both the hydroxyl oxygen atoms yielded similar bond lengths (2.03 and 2.02 Å respectively). For Sys2, a similar energy trend was observed, where coordination *via* O4/O5 atoms gave higher stability, as shown in Mode 5 (Fig. 5b). In terms of bond lengths, both O3′ and O4′ showed higher values in Sys 2, when compared with Sys 1. For the O4–Zn^{2+} bond, an opposite order was observed for Sys2, with Mode 5 exhibiting a slightly greater bond length (1.93 Å) compared to Mode 4 (1.92 Å). An interesting observation to note from Fig. 5a and b is the small energy gap between Site 1 and Site 2 binding. For the mono-nuclear Zn^{2+}, the gap is 3.89 kcal mol^{-1}, which is further reduced to 2.97 kcal mol^{-1} for the bi-nuclear system (Fig. 5b). Hence, there is a slight possibility of an equilibrium distribution between the two arrangements, although further validation is required to justify this. Finally, to compare the band gaps between the frontier molecular orbitals, MO diagrams for HOMO and LUMO, along with their respective energies, were obtained for all five systems, as shown in Fig. 6. For Sys 1, the lowest band gap was observed for Mode 2 (72.40 kcal mol^{-1}), followed by Mode 1 (80.57 kcal mol^{-1}), and then Mode 3 (84.78 kcal mol^{-1}). Similarly, for Sys 2, Mode 5 exhibited a lower band gap (67.22 kcal mol^{-1}) compared to Mode 4 (71.66 kcal mol^{-1}). Hence, a good correlation was observed between the stability of a complex (Fig. 5) and its corresponding band gap, wherein a stable complex yielded a lower band gap between the HOMO and LUMO orbitals. As a lower band gap corresponds to higher reactivity, therefore, the reactivity order in Sys 1 could be Mode 2 > Mode 1 > Mode 3. Similarly, for Sys 2, the order is Mode 5 > Mode 4.

3.8 Detection of $^1O_2$ species

To assess the $^1O_2$ generation capability of ZnQ@Ce6, the absorption changes were monitored for DPBF alone (Fig. 7a), Ce6 + DPBF (Fig. 7b), ZnQ NPs + DPBF (Fig. 7c), ZnQ@Ce6 (Fig. 7d), and ZnQ@Ce6 + DPBF (Fig. 7e) under 635 nm laser irradiation for 0–60 seconds. The absorption spectra of ZnQ NPs + DPBF, DPBF, and ZnQ@Ce6 displayed no significant changes. In contrast, the absorption spectra of Ce6 + DPBF and ZnQ@Ce6 + DPBF exhibited a decrease in the absorbance peak with prolonged irradiation time. This reduction in the DPBF absorption peak indicated its consumption by the gener-

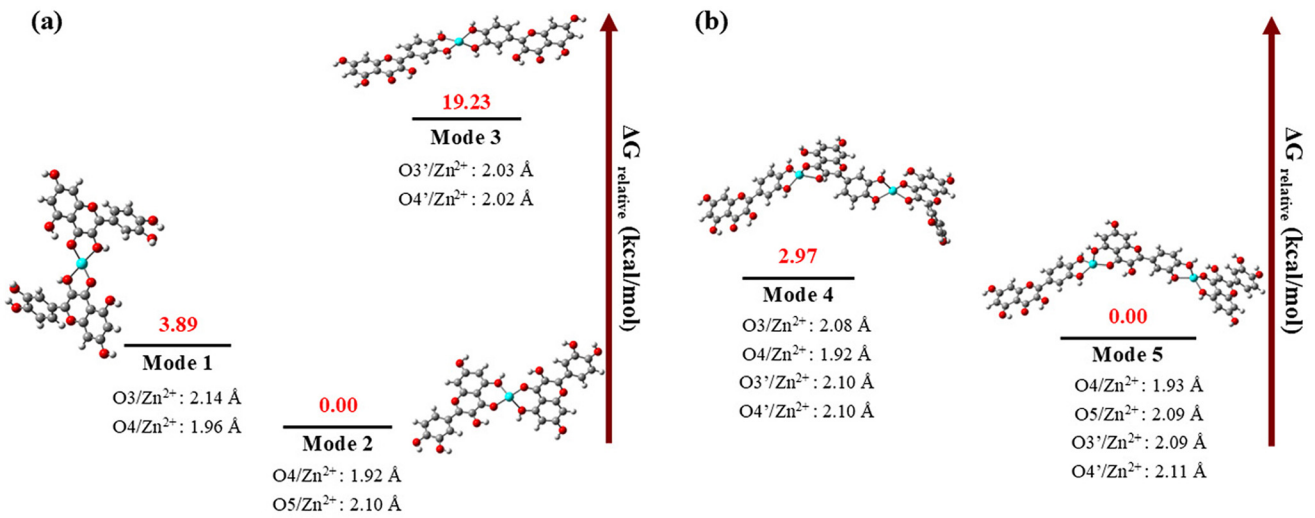

Fig. 5 Relative Δ*G* values, for different binding modes of (a) Sys1 and (b) Sys2.

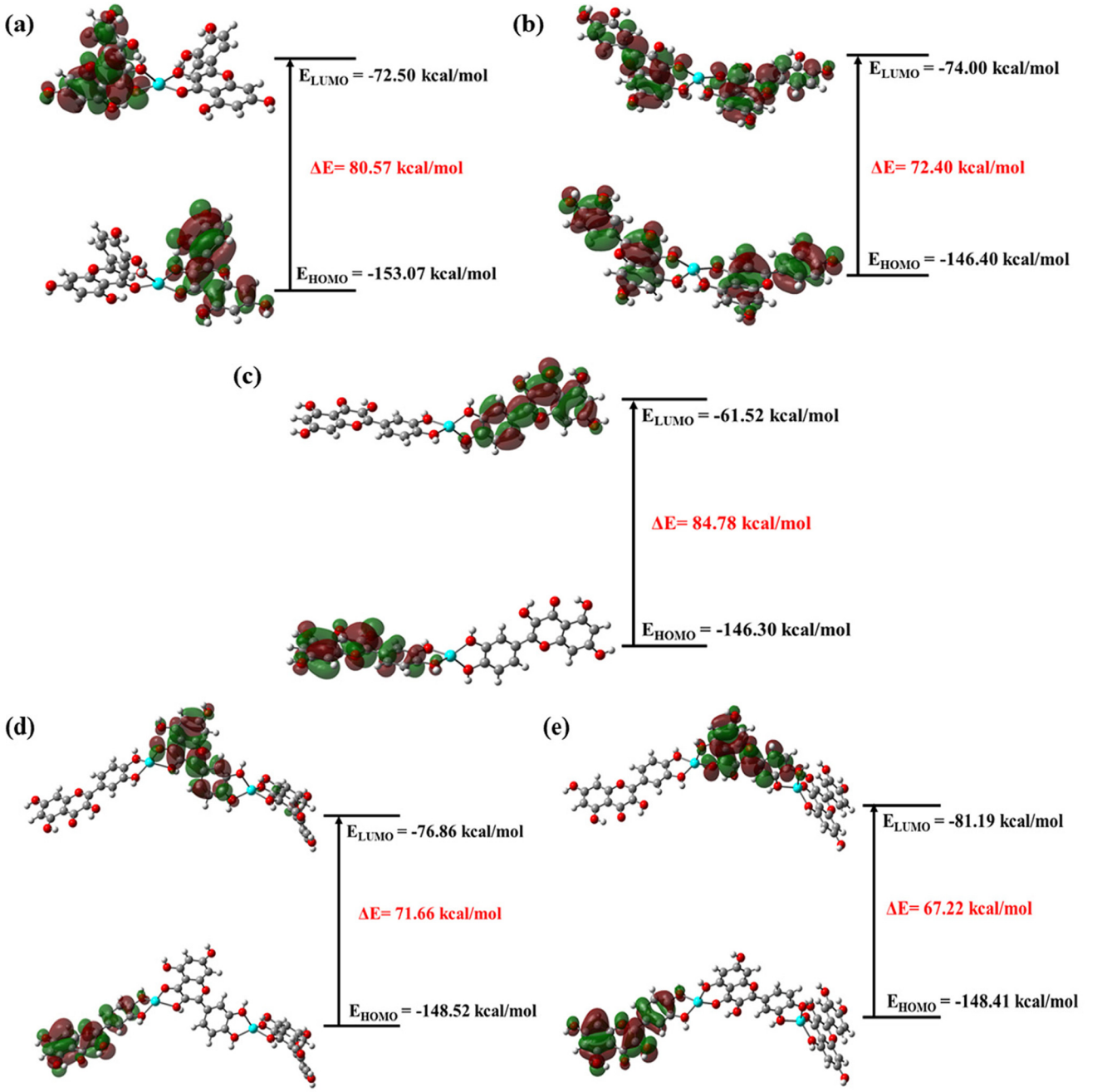

Fig. 6 Frontier Molecular Orbital (FMO) diagrams, along with their associated energy gaps for (a) Mode 1, (b) Mode 2, and (c) Mode 3 of Sys1; the corresponding parameters for (d) Mode 4, and (e) Mode 5 of Sys 2.

ated singlet oxygen ($^1O_2$), demonstrating the effectiveness of ZnQ@Ce6 as a promising PDT agent under 635 nm light irradiation. EPR spectroscopy further confirmed the ability of free Ce6 and ZnQ@Ce6 to generate $^1O_2$ under 635 nm laser irradiation. 2,2,6,6-Tetramethylpiperidine (TEMP) was used as a $^1O_2$ trap. Fig. 7f shows distinct signals corresponding to $^1O_2$-induced TEMP-1-oxyl in the ESR spectra of Ce6 and ZnQ@Ce6, whereas no peak was observed for ZnQ NPs after 5 minutes of laser irradiation.[50] These results demonstrate that ZnQ@Ce6 is an effective PDT agent under light exposure. A comparison with reported combinational chemo-PDT nanocomposites is presented in Table S1.†

3.9 *In vitro* quercetin and Ce6 release studies

To assess the release kinetics of ZnQ@Ce6, the cumulative drug release profiles of quercetin and Ce6 were examined in PBS solutions at pH 7.4 (mimicking physiological conditions) and pH 5.5 (simulating the acidic tumor microenvironment). Quercetin, known for its anti-cancer properties as a flavone, inhibits cancer cell proliferation. Using a UV-vis spectrophoto-

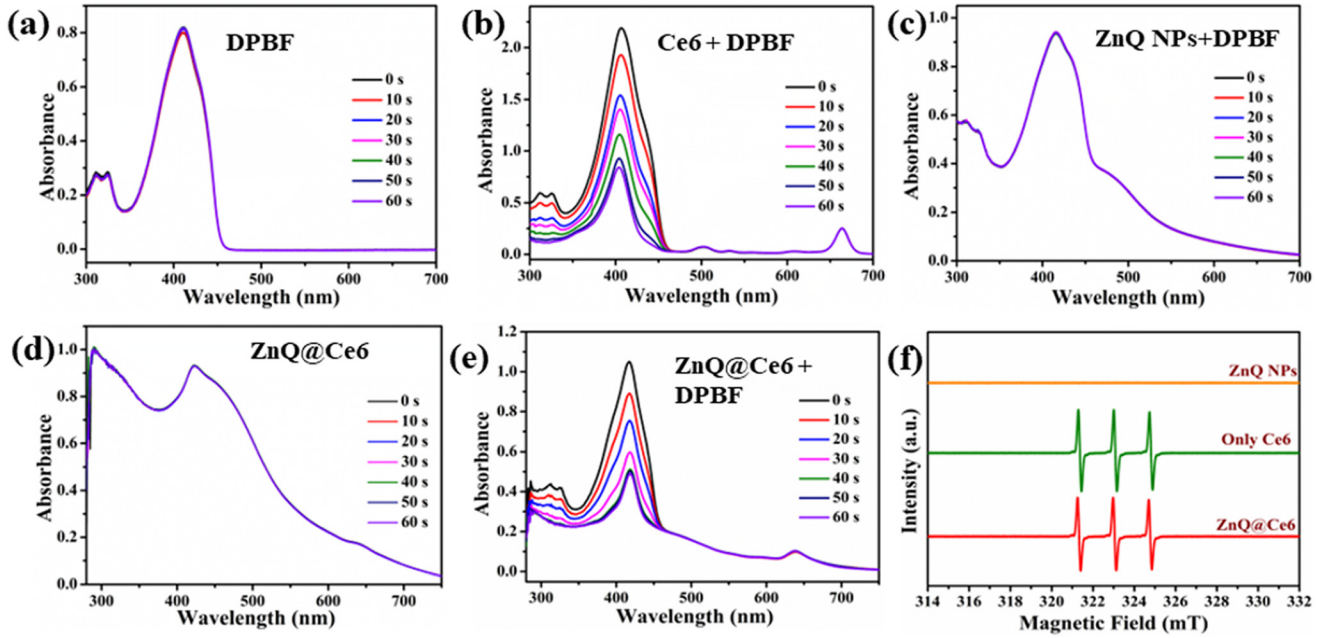

Fig. 7 Changes in the absorption spectra of (a) DPBF, (b) Ce6 + DPBF, (c) ZnQ NPs + DPBF, (d) ZnQ@Ce6, and (e) ZnQ@Ce6 + DPBF, under 635 nm laser. (f) EPR spectra of ZnQ NPs, only Ce6, and ZnQ@Ce6 in the presence of laser irradiation (635 nm laser, 60 mW cm^{-2}, 5 min).

meter, the cumulative drug release percentages of quercetin and Ce6 were determined from their respective absorbance values at 374 nm and 660 nm based on the calibration curves in Fig. S15.† The results in Fig. 8a and b indicate the rapid release of both quercetin and Ce6 within the initial 6 hours, followed by a more gradual release thereafter. This phenom-

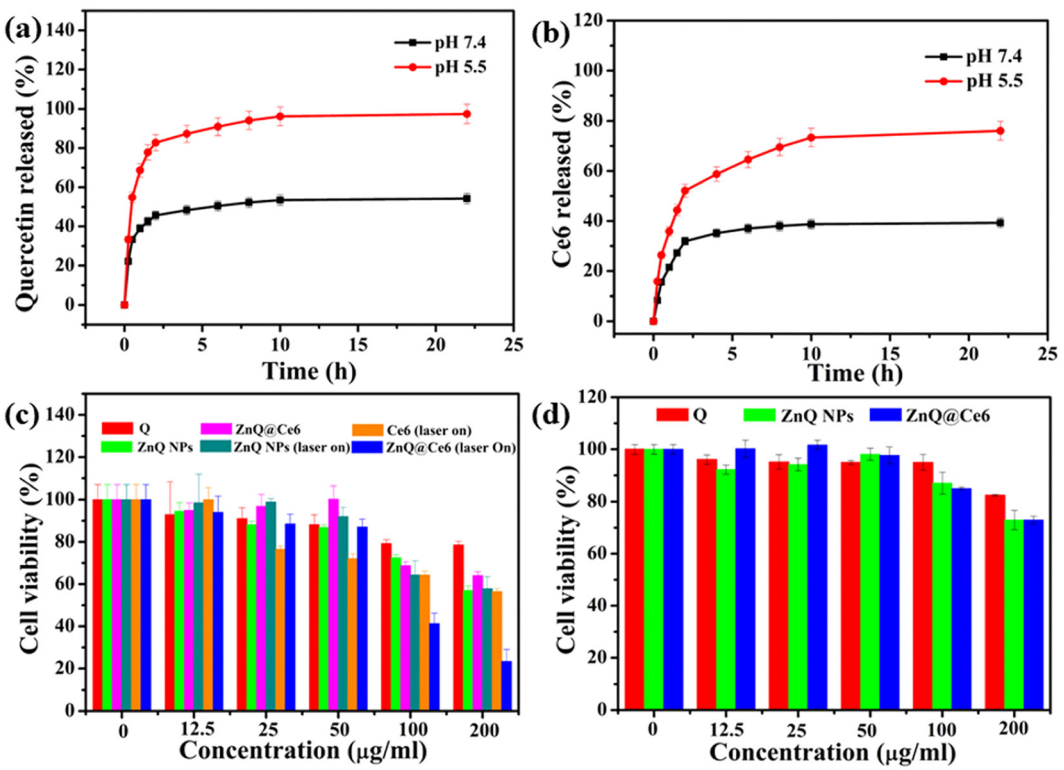

Fig. 8 *In vitro* evaluation of the amount of (a) quercetin and (b) Ce6 released from ZnQ@Ce6 in PBS at pH 7.4 and 5.5, separately for different periods. (c) Cell viability of HeLa cells after incubation with Q (quercetin), ZnQ NPs, Ce6, and ZnQ@Ce6 with and without laser irradiation (635 nm, 60 mW cm^{-2}, 5 min). (d) Cell viability of HEK293T after incubation with Q (quercetin), ZnQ NPs, Ce6, and ZnQ@Ce6.

enon is likely attributable to the swift removal of Ce6 and quercetin molecules from the surface of the NPs. After 22 hours of incubation at pH 5.5, ZnQ@Ce6 released approximately 97.46 ± 4.8% of quercetin and 76.07 ± 3.8% of the loaded Ce6, whereas at pH 7.4, ZnQ@Ce6 released approximately 54.25 ± 4.7% of quercetin and 39.26 ± 3.9% of the loaded Ce6. These findings highlight that quercetin and Ce6 were released more effectively in acidic tumor environments compared to pH 7.4. We investigated the cumulative release under light exposure and found that the nanocomposite ZnQ@Ce6 exhibited sensitivity to low pH both in the dark and under laser irradiation, with no significant changes in release kinetics (Fig. S16†). Thus, we utilized the pH-responsive nature of ZnQ@Ce6 to release drugs under acidic conditions for combinational chemo-photodynamic therapy.

3.10 MTT assay

The cytotoxicity evaluation of quercetin, Ce6, ZnQ NPs, and ZnQ@Ce6 was conducted in HeLa cells with various concentrations (0, 12.5, 25, 50, 100, and 200 μg ml^{-1}) in the presence and absence of laser irradiation. The MTT test results given in Fig. 8c and d revealed that quercetin, ZnQ NPs, and ZnQ@Ce6 inhibited cell growth in a dose-dependent manner, significantly reducing the cancer cell viability at concentrations of 100 and 200 μg ml^{-1}. A comparison of the cytotoxicity between free quercetin and ZnQ NPs/ZnQ@Ce6 formulations indicated that lower concentrations of ZnQ NPs and ZnQ@Ce6 were required to achieve similar cytotoxic effects to free quercetin. This suggests that the cellular toxicity of quercetin increased when delivered through ZnQ NPs and ZnQ@Ce6 formulations. The cell viability of ZnQ NPs remained unchanged with or without laser irradiation, as no singlet oxygen ($^1O_2$) was generated. However, HeLa cells treated with Ce6 and ZnQ@Ce6 exhibited dose-dependent inhibition when exposed to a 635 nm laser for 5 minutes. Furthermore, upon exposure to a 635 nm laser for 5 minutes, both ZnQ@Ce6 and free Ce6 showed significant cell inhibition rates at concentrations of 100 and 200 μg ml^{-1}. After 24 hours of incubation, only 56% of HeLa cells survived at a Ce6 concentration of 200 μg ml^{-1}, while only 23% of cells survived when treated with ZnQ@Ce6 at the same concentration. This higher cell inhibition rate with ZnQ@Ce6 may be attributed to the combined effect of the anticancer drug quercetin and the generation of cytotoxic $^1O_2$ by Ce6. Additionally, an MTT assay in HEK293T cells was conducted, showing approximately 70% cell viability at the maximum concentration. These results collectively validate the dual-mode anticancer efficacy of ZnQ@Ce6, acting as both a drug nanocarrier and an effective PDT agent.

3.11 Intracellular uptake study

The time-dependent cellular internalization study of ZnQ@Ce6 was evaluated in the HeLa cell line through an *in vitro* study, and fluorescence images were captured using a Leica fluorescence microscope image, as depicted in Fig. 9. The cells were incubated for various time durations (1.5 h, 3 h, 6 h, and 12 h). DAPI staining (blue fluorescence) was employed for nuclei labeling, and the red emission stemmed from the Ce6 incorporated within ZnQ@Ce6. Merged images of both channels were presented accordingly. The images revealed the predominant localization of ZnQ@Ce6 (red fluorescence) in the cytoplasm. Initially, a weak red fluorescent signal from ZnQ@Ce6 was observed after 0.5 h of cellular uptake by HeLa cells, suggesting that only a limited number of ZnQ@Ce6 nanoparticles penetrated the cells in the 0.5 h duration. However, as expected, the fluorescence intensity increased over time, indicating the progressive uptake of NPs by cancer cells, as evidenced by the escalating red emission in the fluorescence microscopy images. Complete uptake was observed after a 12 hour coincubation period. The internalization study of ZnQ@Ce6 was then compared with that of the free Ce6 molecule, as illustrated in Fig. S17.† The comparison revealed that the fluorescence of Ce6 was not quenched upon loading onto ZnQ NPs.

3.12 *In vitro* $^1O_2$ generation study of ZnQ@Ce6

The evaluation of singlet oxygen production was conducted using DCFH-DA (excitation = 488 nm, emission = 530 nm) as the ROS indicator across five experimental groups: (i) DCFH-DA, (ii) DCFH-DA + $h\nu$, (iii) Ce6 + DCFH-DA + $h\nu$, (iv) ZnQ@Ce6 + DCFH-DA, and (v) ZnQ@Ce6 + DCFH-DA + $h\nu$. Non-irradiated cells in groups (i) and (iv) exhibited no green fluorescence in the absence of laser irradiation, indicating negligible toxicity from ZnQ@Ce6, and DCFH-DA as no singlet oxygen was produced (see Fig. 10). However, group (ii) showed no fluorescence post-exposure to a 635 nm laser for 5 minutes, while groups (iii) and (v) displayed green fluorescence, confirming the formation of DCF and the inability of DCFH-DA to generate $^1O_2$ in the presence of light. In contrast, free Ce6 and ZnQ@Ce6 effectively produced $^1O_2$ when exposed to light irradiation. Quantitative analysis (Fig. S18†) revealed that ZnQ@Ce6 treated cells exhibited 1.35 times higher fluorescence intensity than those incubated with free Ce6. Notably, free Ce6 induced a moderate green fluorescence, indicating its cellular uptake and ROS generation capability. Furthermore, ultra-high fluorescence signal intensity was observed in the cells treated with ZnQ@Ce6, demonstrating its superior ROS production capacity. Concurrently, we observed the cells contracting to a spherical shape, confirming HeLa cell death induced by singlet oxygen generation. Furthermore, as a control experiment, we irradiated the cells without ZnQ@Ce6 and observed no change in the cell morphology after 2 minutes of laser exposure, as shown in Fig. S19.† These findings collectively highlight the minimal toxicity of ZnQ@Ce6 in the absence of laser and its toxicity upon exposure to laser irradiation due to singlet oxygen production.

3.13 *In vitro* therapeutic effect

To determine the *in vitro* therapeutic effects of ZnQ@Ce6, a calcein-AM/EthD-III double-staining assay was conducted to assess the antitumor activity of HeLa cells across five experimental groups.[51] Following the incubation of cancer cells under various treatment conditions, calcein AM (CM) and

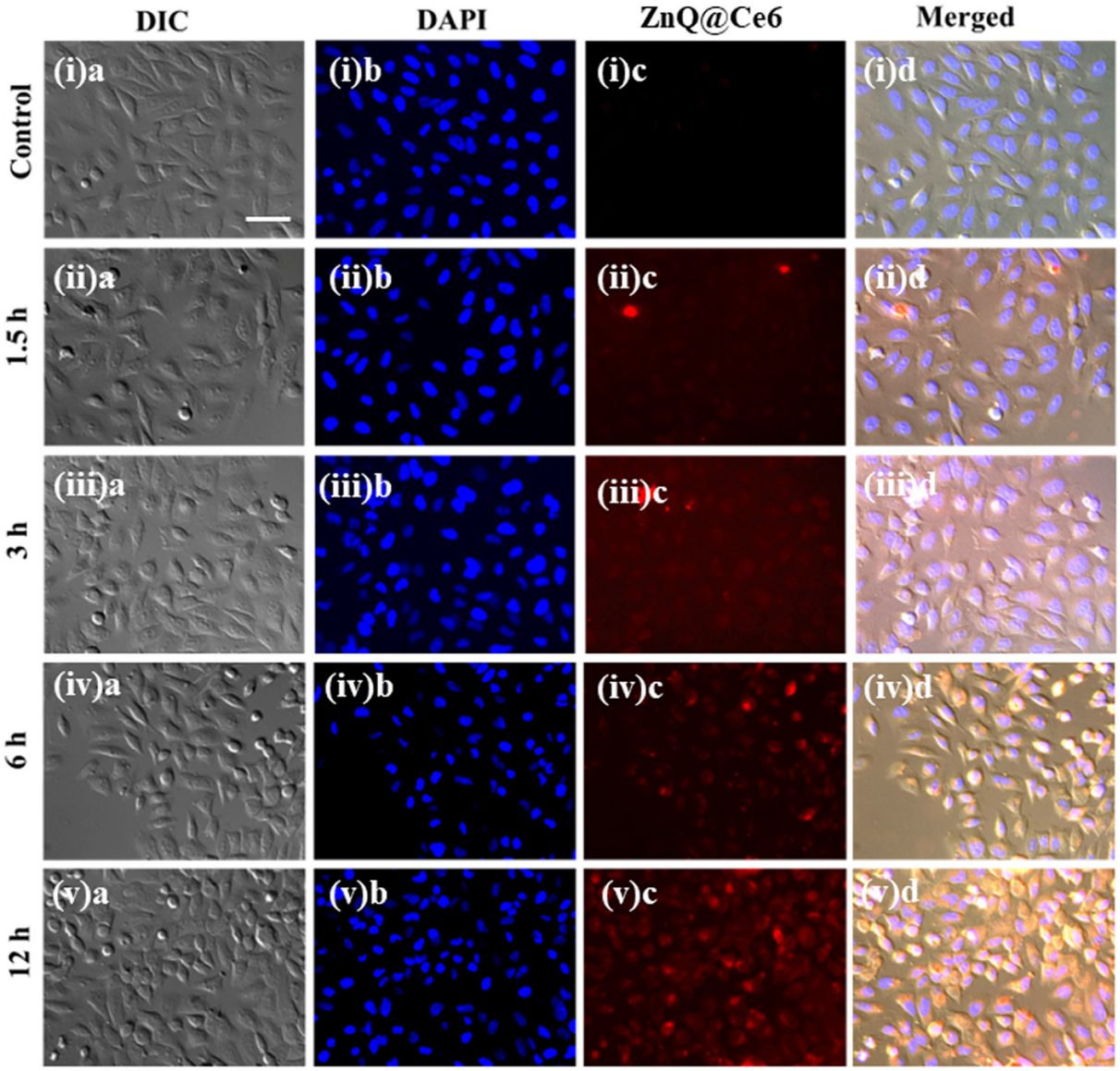

Fig. 9 Cellular internalization of ZnQ@Ce6: (a) Differential Interference Contrast (DIC), (b) DAPI nuclei labeling, (c) ZnQ@Ce6, and (d) merged images at various time frames – (i) 0 h, (ii) 1.5 h, (iii) 3 h, (iv) 6 h, and (v) 12 h – in HeLa Cells (scale bar: 50 μm).

EthD-III were used for co-staining to distinguish living cells and dead cells, respectively. As depicted in Fig. 11, minimal cell death was observed in both the control group and the *hν* group. The slight red fluorescence intensity indicating dead cells in the ZnQ@Ce6 group was attributed to cell death resulting solely from the release of quercetin in the absence of light. In the Ce6 + *hν* group, the presence of red fluorescence indicated that some HeLa cells died due to the singlet oxygen generation ability of Ce6 upon irradiation. Significantly, the red fluorescence intensity of dead cells in the ZnQ@Ce6 + *hν* group surpassed that of the other groups, suggesting that the combined treatment with nanoparticles containing both quercetin and Ce6 was more effective than the treatment with ZnQ@Ce6 alone or Ce6 + *hν*. This observation indicates the near-complete eradication of cancer cells under this combined treatment regimen.

The flow cytometry results in Fig. S20† indicated that most cells treated with ZnQ@Ce6 + laser underwent apoptosis rather than necrosis. The analysis revealed that the percentage of apoptotic cells in the ZnQ@Ce6 + laser group was greater than those in the other treatment groups. Furthermore, the total cell death, which includes both necrosis and apoptosis, was also greater in the ZnQ@Ce6 + laser group (13.9% + 16.4%) compared to the other groups. These findings were consistent with the outcomes of the MTT assay and the calcein-AM/EthD-III double-staining assay. This indicates that the ZnQ@Ce6 nanocomposite is highly effective in cancer treatment, leading to maximum cell death.

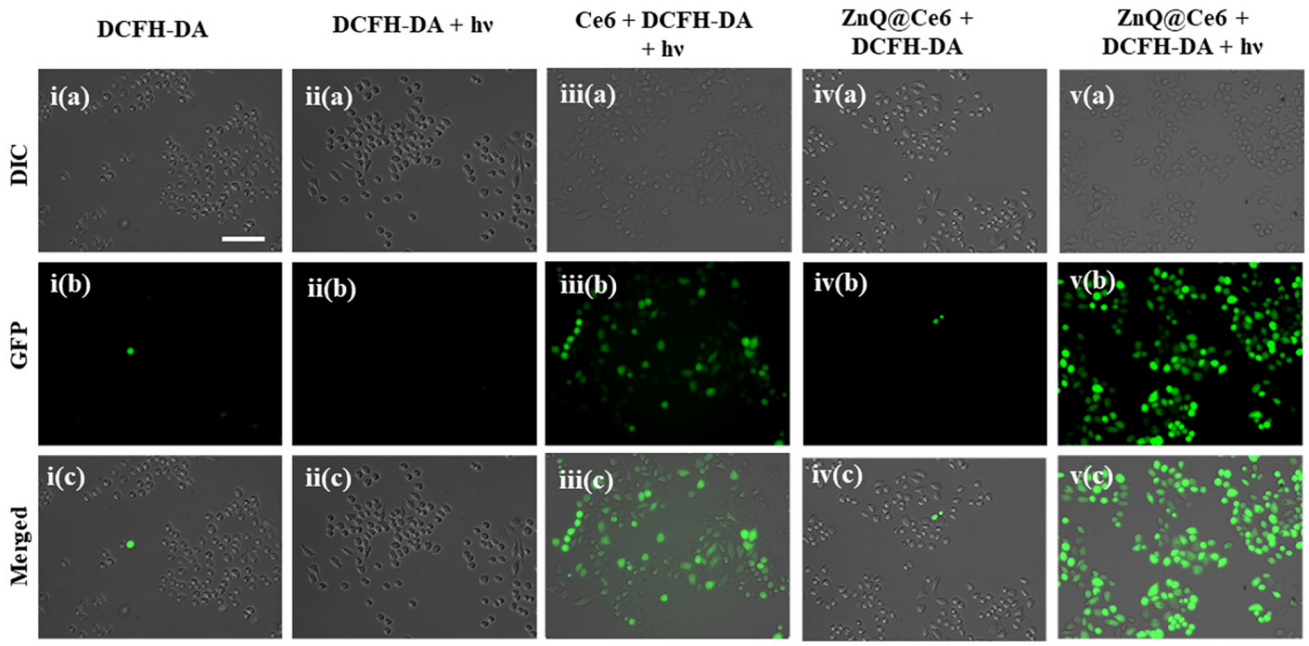

Fig. 10 Singlet oxygen production was determined using DCFH-DA: (a) DIC, (b) GFP, and (c) merged field images for (i) DCFH-DA, (ii) DCFH-DA + $h\nu$, (iii) Ce6 + DCFH-DA + $h\nu$, (iv) ZnQ@Ce6 + DCFH-DA, and (v) ZnQ@Ce6 + DCFH-DA + $h\nu$ in HeLa cells (sScale bar = 100 μm).

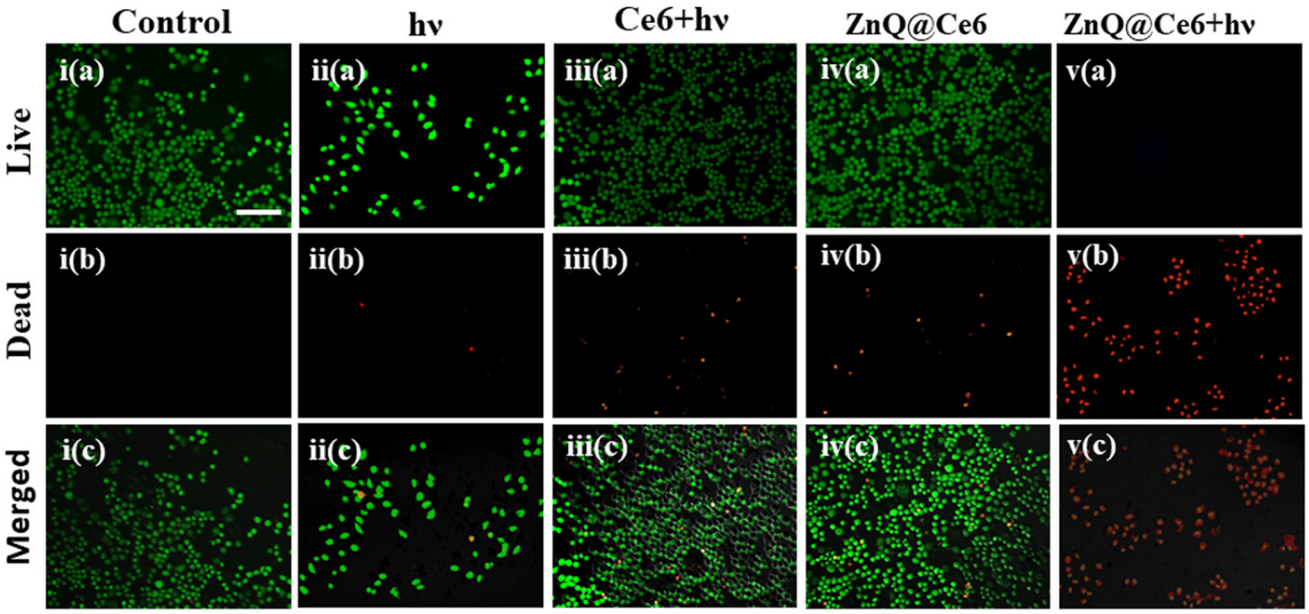

Fig. 11 Calcein-AM/EthD-III double staining of HeLa cells: (a) live, (b) dead, (c) merged after different treatments – (i) control, (ii) $h\nu$, (iii) Ce6 + $h\nu$, (iv) ZnQ@Ce6, and (v) ZnQ@Ce6 + $h\nu$ (scale bar = 100 μm).

4. Conclusion

In summary, we successfully synthesized multifunctional self-assembled ZnQ NPs using quercetin, exploiting its anticancer properties to enhance the therapeutic efficacy through combined chemotherapy and PDT for the first time. The disordered structure of the NPs facilitates more controlled and sustained drug release, crucial for maintaining therapeutic drug levels over extended periods. DFT calculations identified the optimal binding configuration involving O4/O5 coordination with Zn^{2+}, supported by a reduced band gap between FMOs in this arrangement. Ce6 was loaded onto ZnQ NPs addressing the issue of Ce6 agglomeration thereby improving the PDT efficiency. The synthesized ZnQ@Ce6 produced

singlet oxygen ($^1O_2$) under 635 nm laser irradiation, resulting in significant cell killing of 77% at a dose of 200 μg ml^{-1}, compared to 44% cell inhibition with Ce6 alone. This increased efficacy is attributed to the synergistic effect of combining chemotherapy with PDT. Hence, these pH-responsive nanocarriers show significant promise in facilitating combinational chemo-PDT, offering an effective approach for improving therapeutic outcomes for cancer treatment.

Data availability

The data supporting this article have been included as part of the ESI.†

Conflicts of interest

There are no conflicts to declare.

Acknowledgements

K. Negi acknowledges the Prime Minister's Research Fellowship (PMRF) for the scholarship and research grant. This work received financial support from MoE-STARS/STARS-2/2023-0340. The authors are grateful to the Central Research Facility, Indian Institute of Technology (Indian School of Mines) Dhanbad, for HRTEM, FESEM, XPS, BET, XRD, and cell culture studies. K. Negi expresses appreciation to the Department Research Facility of the Department of Chemistry and Chemical Biology, Indian Institute of Technology (Indian School of Mines) Dhanbad, for FTIR analysis. K. Negi is thankful to Dr Umakanta Tripathy and Nitesh Kumar Pathak, Biophysics Laboratory, Department of Physics, ISM for providing the 635 nm laser source. Furthermore, K. Negi extends thanks to STIC, Cochin University of Science and Technology, for the TGA analysis, and Shiv Nadar University, Delhi NCR, for the EPR study.

References

1 R. L. Siegel, K. D. Miller, N. S. Wagle and A. Jemal, *Ca-Cancer J. Clin.*, 2023, **73**, 17–48.
2 S. Liang, X. Deng, P. Ma, Z. Cheng and J. Lin, *Adv. Mater.*, 2020, **32**, 20032114.
3 X. Chen, D. Cheng, M. Ding, N. Yu, J. Liu, J. Li and L. Lin, *J. Mater. Chem. B*, 2022, **10**, 4595–4604.
4 H. Chu, Y. Li, C. Wang, J. W. Shen and Y. Wei, *Dalton Trans.*, 2022, **51**, 16336–16343.
5 Y. Zhou, X. Ren, Z. Hou, N. Wang, Y. Jiang and Y. Luan, *Nanoscale Horiz.*, 2021, **6**, 120–131.
6 M. Zhang, W. Wang, Y. Cui, N. Zhou and J. Shen, *ACS Biomater. Sci. Eng.*, 2018, **4**, 151–162.
7 C. Xu and K. Pu, *Chem. Soc. Rev.*, 2021, **50**, 1111–1137.
8 S. S. Lucky, K. C. Soo and Y. Zhang, *Chem. Rev.*, 2015, **115**, 1990–2042.
9 J. Chen, T. Fan, Z. Xie, Q. Zeng, P. Xue, T. Zheng, Y. Chen, X. Luo and H. Zhang, *Biomaterials*, 2020, **237**, 119827.
10 Q. Huang, Y. Chen, M. Ye, S. Zhuang, A. Zhong, J. Liu, G. Maduraiveeran, Y. Peng and Y. Huang, *Mater. Today Chem.*, 2024, **40**, 102235.
11 Y. Deng, M. Guo, L. Zhou, Y. Huang, S. Srivastava, A. Kumar and J. Q. Liu, *Biomater. Sci.*, 2024, **12**, 3725–3744.
12 C. Jiang, L. Zhou, W. Hu, J. Luo, A. Nezamzadeh-Ejhieh, J. Ouyang, X. Liu, Y. Pan, S. Cui and J. Liu, *Mater. Today Chem.*, 2024, **36**, 101964.
13 J. Hu, Z. Xu, D. Liao, Y. Jiang, H. Pu, Z. Wu, X. Xu, Z. Zhao, J. Liu, X. Lu and X. Liu, *Adv. Healthcare Mater.*, 2023, **12**, 2301316.
14 A. Murakami, H. Ashida and J. Terao, *Cancer Lett.*, 2008, **269**, 315–325.
15 M. Ezzati, B. Yousefi, K. Velaei and A. Safa, *Life Sci.*, 2020, **248**, 117463.
16 S. Srivastava, R. R. Somasagara, M. Hegde, M. Nishana, S. K. Tadi, M. Srivastava, B. Choudhary and S. C. Raghavan, *Sci. Rep.*, 2016, **6**, 24049.
17 M. Parsaei and K. Akhbari, *Inorg. Chem.*, 2022, **61**, 19354–19368.
18 M. Matiyani, A. Rana, M. Pal, S. Rana, A. B. Melkani and N. G. Sahoo, *RSC Adv.*, 2022, **12**, 2574–2588.
19 Y. Zhang, S. Gong, L. Liu, H. Shen, E. Liu, L. Pan, N. Gao, R. Chen and Y. Huang, *ACS Appl. Mater. Interfaces*, 2023, **15**, 40228–40240.
20 W. Jiang, H. Zhang, J. Wu, G. Zhai, Z. Li, Y. Luan and S. Garg, *ACS Appl. Mater. Interfaces*, 2018, **10**, 34513–34523.
21 M. Parsaei and K. Akhbari, *Inorg. Chem.*, 2022, **61**, 14528–14543.
22 H. V. T. Nguyen, S. N. Pham, A. Mirzaei, N. X. D. Mai, C. C. Nguyen, H. T. Nguyen, L. B. Vong, P. T. Nguyen and T. L. H. Doan, *Colloids Surf., A*, 2024, **696**, 134288.
23 X. Meng, J. Deng, F. Liu, T. Guo, M. Liu, P. Dai, A. Fan, Z. Wang and Y. Zhao, *Nano Lett.*, 2019, **19**, 7866–7876.
24 D. Wang, H. Wu, S. Z. F. Phua, G. Yang, W. Q. Lim, L. Gu, C. Qian, H. Wang, Z. Guo, H. Chen and Y. Zhao, *Nat. Commun.*, 2020, **11**, 357.
25 J. Ni, X. Yin, S. Liao, M. Cai, R. Zhu, T. Fu, Y. Du, J. Kong, Y. Zhang, C. Qu and X. Dong, *Mol. Pharmaceutics*, 2023, **20**, 875–885.
26 X. Fu, Z. Yang, T. Deng, J. Chen, Y. Wen, X. Fu, L. Zhou, C. Yu and Z. Zhu, *J. Mater. Chem. B*, 2020, **8**, 1481–1488.
27 S. Sheng, F. Liu, L. Lin, N. Yan, Y. Wang, C. Xu, H. Tian and X. Chen, *J. Controlled Release*, 2020, **328**, 631–639.
28 W. L. Jia, B. Jin, W. J. Xu, S. W. Liu, X. Y. Mao, H. Peng and Y. W. Zhang, *ACS Appl. Mater. Interfaces*, 2023, **15**, 50069–50082.
29 P. Mukherjee, S. Tripathy, M. G. Matsabisa and S. K. Sahu, *J. Photochem. Photobiol., A*, 2023, **437**, 114426.
30 P. Yadav, P. Bhardwaj, M. Maruthi, A. Chakraborty and P. Kanoo, *Dalton Trans.*, 2023, **52**, 11725–11734.

31 M. J. Frisch, G. W. Trucks, H. B. Schlegel, G. E. Scuseria, M. A. Robb, J. R. Cheeseman, G. Scalmani, V. Barone, G. A. Petersson, H. Nakatsuji, X. Li, M. Caricato, A. V. Marenich, J. Bloino, B. G. Janesko, R. Gomperts, B. Mennucci, H. P. Hratchian, J. V. Ortiz, A. F. Izmaylov, J. L. Sonnenberg, D. Williams-Young, F. Ding, F. Lipparini, F. Egidi, J. Goings, B. Peng, A. Petrone, T. Henderson, D. Ranasinghe, V. G. Zakrzewski, J. Gao, N. Rega, G. Zheng, W. Liang, M. Hada, M. Ehara, K. Toyota, R. Fukuda, J. Hasegawa, M. Ishida, T. Nakajima, Y. Honda, O. Kitao, H. Nakai, T. Vreven, K. Throssell, J. A. Montgomery Jr, J. E. Peralta, F. Ogliaro, M. J. Bearpark, J. J. Heyd, E. N. Brothers, K. N. Kudin, V. N. Staroverov, T. A. Keith, R. Kobayashi, J. Normand, K. Raghavachari, A. P. Rendell, J. C. Burant, S. S. Iyengar, J. Tomasi, M. Cossi, J. M. Millam, M. Klene, C. Adamo, R. Cammi, J. W. Ochterski, R. L. Martin, K. Morokuma, O. Farkas, J. B. Foresman and D. J. Fox, *Gaussian 16 Rev. C.01*, 2016.
32 A. D. Becke, *J. Chem. Phys.*, 1993, **98**, 5648–5652.
33 C. Lee, W. Yang and R. G. Parr, *Phys. Rev. B: Condens. Matter Mater. Phys.*, 1988, **37**, 785–789.
34 S. Grimme, S. Ehrlich and L. Goerigk, *J. Comput. Chem.*, 2011, **32**, 1456–1465.
35 R. Ditchfield, W. J. Hehre and J. A. Pople, *J. Chem. Phys.*, 1971, **54**, 724–728.
36 R. Krishnan, J. S. Binkley, R. Seeger and J. A. Pople, *J. Chem. Phys.*, 1980, **72**, 650–654.
37 P. C. Hariharan and J. A. Pople, *Theor. Chim. Acta*, 1973, **28**, 213–222.
38 P. J. Hay and W. R. Wadt, *J. Chem. Phys.*, 1985, **82**, 270–283.
39 S. Miertus, E. Scrocco and J. Tomasi, *Chem. Phys.*, 1981, **55**, 117–129.
40 K. Negi, N. K. Pathak, U. Tripathy, S. K. Dey and S. K. Sahu, *Colloids Surf., A*, 2024, **694**, 134163.
41 T. S. de Castilho, T. B. Matias, K. P. Nicolini and J. Nicolini, *Food Sci. Hum. Wellness*, 2018, **7**, 215–219.
42 O. O. Ojo, D. I. Fatokun, I. P. Ejidike, R. U. Awolope and S. O. Sanni, *J. Toxicol.*, 2022, **1**, 6178261.
43 X. Chen, D. J. McClements, Y. Zhu, Y. Chen, L. Zou, W. Liu, C. Cheng, D. Fu and C. Liu, *Food Res. Int.*, 2018, **114**, 30–37.
44 E. Halevas, B. Mavroidi, M. Pelecanou and A. G. Hatzidimitriou, *Inorg. Chim. Acta*, 2021, **523**, 120407.
45 A. A. Andelescu, C. Cretu, V. Sasca, S. Marinescu, L. Cseh, O. Costisor and E. I. Szerb, *Polyhedron*, 2018, **147**, 120–125.
46 A. Kumar, K. Negi and S. K. Sahu, *New J. Chem.*, 2024, **48**, 7265–7276.
47 M. Parsaei and K. Akhbari, *ACS Omega*, 2023, **8**, 41321–41338.
48 R. Kumari, A. Kumar, K. Negi and S. K. Sahu, *ACS Appl. Nano Mater.*, 2023, **6**, 918–929.
49 L. X. Gao, Y. L. Ji, W. L. Bi, A. Tang and Y. Tian, *ACS Appl. Nano Mater.*, 2023, **6**, 15054–15062.
50 Q. Xiang, W. Li, Y. Tan, J. Shi, M. Dong, J. Cheng, J. Huang, W. Zhang, Y. Gong, Q. Yang, L. Yang, H. Dong and X. Zhang, *Chem. Eng. J.*, 2022, **444**, 136706.
51 S. Wang, M. Ma, Q. Liang, X. Wu, K. Abbas, J. Zhu, Q. Xu, A. C. Tedesco and H. Bi, *ACS Appl. Nano Mater.*, 2022, **5**, 6679–6690.